Tensile-strain effects in quantum-well and superlattice band structures

Arvind Baliga, Dhrupad Trivedi, and Neal G. Anderson
Department of Electrical and Computer Engineering, University of Massachusetts at Amherst, Amherst, Massachusetts 01003
(Received 26 August 1993; revised manuscript received 20 December 1993)

The effects of tensile strain on the energy-band structures of semiconductor quantum wells and superlattices (SL's) are studied theoretically, with emphasis on structures with unique valence-subband configurations achievable only through the use of tensile strain. Quantum wells are treated using finite-element envelope-function calculations which fully treat interactions between the light-hole, heavy-hole, and split-off valence bands, whereas strained SL's are modeled using a superlattice $\mathbf{K}\cdot\mathbf{p}$ approach modified to treat strain effects. The two models are described in detail, tested for appropriate cases where both models should be applicable, and applied to prototype structures based on the III-V $GaAs_{1-x}P_x/Al_yGa_{1-y}As$ and $In_xGa_{1-x}As/InP$ heterostructure systems. Single quantum wells are considered first. Transition energies are calculated and conveniently plotted as functions of composition (or strain) and layer thickness for both systems, and valence-subband band structures and $\mathbf{k}$-dependent optical matrix elements are examined in detail for both systems in regimes where crossing of the uppermost light- and heavy-hole bands is induced by composition or well-width changes. Superlattices in both material systems are then considered, with emphasis on structures in which crossing of the uppermost valence subbands is induced by variation of barrier width. Band structures and optical matrix elements are calculated for wave vectors along directions parallel and perpendicular to the layer planes both in free-standing $GaAs_{1-x}P_x/Al_yGa_{1-y}As$ SL's with strain shared between the well and barrier layers and $In_xGa_{1-x}As/InP$ SL's strained to lattice match to InP substrates. Finally, general features of band structures and optical matrix elements in tensile-strained structures inferred from these studies are summarized. Implications for tensile-strained quantum-well lasers are discussed briefly.

I. INTRODUCTION

Tensile-strain effects in layered heterostructures offer unprecedented flexibility for band-structure engineering in quantum wells and superlattices, providing more degrees of freedom than are available in lattice matched or compressively strained systems. The splitting between the uppermost light- and heavy-hole valence subbands can be eliminated through careful manipulation of tensile-strain and quantum-size effects in these structures ("merged" configuration), and the normal ordering of the uppermost subbands can even be reversed so the light-hole valence subband lies at the highest energy ("light-hole-up" configuration).[1] This is interesting from a fundamental point of view, and has proven useful for optoelectronic device applications as well. Semiconductor lasers based on tensile-strained quantum wells have received considerable attention recently,[2] as have polarization-insensitive optical amplifiers[3] and phase modulators[4] and Stark-effect modulators exhibiting enhanced low-field electroabsorption.[5]

In this work, we theoretically explore the effects of tensile strain on the energy-band structures of semiconductor quantum wells (QW's) and strained-layer superlattices (SLS's). We focus specifically on structures with unique valence-subband configurations achievable only through the use of tensile strain, i.e., structures in which merged or light-hole-up valence-band configurations are obtained. Using finite-element and superlattice $\mathbf{K}\cdot\mathbf{p}$ models for strained QW's and SLS's, respectively, we examine $GaAs_{1-x}P_x/Al_yGa_{1-y}As$ and $In_xGa_{1-x}As/InP$ structures in which valence-band configurations can be tuned through the merger point by variation of quantum-well alloy compositions, quantum-well thicknesses, or—in superlattices—barrier layer thicknesses. Growth on $\langle 100\rangle$ substrates is assumed for all structures.

Our paper is organized as follows: In Section II, the finite-element and superlattice $\mathbf{K}\cdot\mathbf{p}$ models are described in detail, and results from the two models are compared for appropriate cases where both models should be valid (i.e., isolated quantum wells). Results from finite-element calculations for isolated quantum wells with unstrained barriers are presented next in Sec. III A. Calculated well-width dependence of electron–light-hole (e-lh) and electron–heavy-hole (e-hh) optical transition energies in $GaAs_{1-x}P_x/Al_{0.35}Ga_{0.65}As$ and $In_xGa_{1-x}As/InP$ structures of various alloy compositions are presented first. Valence-subband band structures and wave-vector-dependent optical matrix elements are then examined in detail for both systems in regimes where crossing of the uppermost light- and heavy-hole bands are induced by quantum-well composition or thickness changes. Superlattices in both material systems are considered next in Sec. III B, with emphasis on structures in which crossing of the uppermost valence subbands is induced by variation of barrier width alone. Band structures and optical matrix elements are calculated for wave vectors along directions parallel and perpendicular to the layer planes both in free-standing $GaAs_{1-x}P_x/Al_yGa_{1-y}As$ SL's with strain shared between the well and barrier layers and $In_xGa_{1-x}As/InP$ structures lattice matched to InP substrates. Valence-band crossing is shown to be achiev-

0163-1829/94/49(15)/10402(15)/$06.00 ©1994 The American Physical Society

able solely through barrier-width variations in both types of structures. In Sec. IV, we summarize the general features of tensile-strain effects on QW and SLS band structures and optical matrix elements, and mention some implications of our work for tensile-strained laser design. Our models and results should be useful for a variety of studies involving tensile-strained quantum structures.

II. THEORETICAL MODELS

A. General

Both of the models used in this study are based on envelope-function approaches.[6] Such approaches involve matrix solution of Schrodinger's equation using Bloch-like basis functions of the form

$$|\nu,\mathbf{k}\rangle = u_\nu(\mathbf{r})\exp(i\mathbf{k}\cdot\mathbf{r}) , \tag{1}$$

where $\mathbf{k}$ is the electron wave vector, $\mathbf{r}$ is the position vector, and u_ν is the cell-periodic component (assumed $\mathbf{k}$ independent) for band ν. These functions, while not true Bloch functions, approximately describe bulk band states near the Brillouin-zone center. Functions u_ν typically used to construct a basis set adequate for describing near-gap heterostructure states are, in angular momentum notation $|J,M_J\rangle$,

$$|\tfrac{1}{2},+\tfrac{1}{2}\rangle_c = |S\uparrow\rangle , \tag{2}$$

$$|\tfrac{1}{2},-\tfrac{1}{2}\rangle_c = |S\downarrow\rangle , \tag{3}$$

for the conduction bands,

$$|\tfrac{3}{2},+\tfrac{3}{2}\rangle = (1/\sqrt{2})|(X+iY)\uparrow\rangle , \tag{4}$$

$$|\tfrac{3}{2},-\tfrac{3}{2}\rangle = -(1/\sqrt{2})|(X-iY)\downarrow\rangle , \tag{5}$$

for the heavy-hole bands,

$$|\tfrac{3}{2},+\tfrac{1}{2}\rangle = (1/\sqrt{6})|(X+iY)\downarrow\rangle - \sqrt{\tfrac{2}{3}}|Z\uparrow\rangle , \tag{6}$$

$$|\tfrac{3}{2},-\tfrac{1}{2}\rangle = -(1/\sqrt{6})|(X-iY)\uparrow\rangle - \sqrt{\tfrac{2}{3}}|Z\downarrow\rangle , \tag{7}$$

for the light-hole bands, and

$$|\tfrac{1}{2},+\tfrac{1}{2}\rangle = (1/\sqrt{3})|(X+iY)\downarrow\rangle + (1/\sqrt{3})\,|Z\uparrow\rangle , \tag{8}$$

$$|\tfrac{1}{2},-\tfrac{1}{2}\rangle = (1/\sqrt{3})|(X-iY)\uparrow\rangle - (1/\sqrt{3})|Z\downarrow\rangle , \tag{9}$$

for the split-off bands. Here J and M_J are the total and azimuthal angular momentum quantum numbers, X, Y, Z, and S represent functions with the symmetries of atomic p_x, p_y, p_z, and s orbitals, respectively, and $\uparrow$ and $\downarrow$ denote spin-up and spin-down states. These basis functions diagonalize the "unperturbed" bulk crystal Hamiltonian at $\mathbf{k}=\mathbf{0}$, including both the $\mathbf{k}\cdot\mathbf{p}$ interaction and the valence-band spin-orbit interaction. The 8×8 Hamiltonian matrix constructed from these functions describes interactions between the various bulk band states such as those arising from the $\mathbf{k}\cdot\mathbf{p}$ interaction, internal potentials induced by band offsets at heterointerfaces, and additional potentials arising from other internal and externally applied perturbations. Particular interactions expected to be small are typically neglected to make the Hamiltonian matrix more sparse and/or decouple it into smaller blocks.

In this work, strained single quantum wells (SQW's) are treated by constructing an 8×8 Hamiltonian matrix which includes all $\mathbf{k}\cdot\mathbf{p}$ and strain interactions except those which couple the conduction bands (CB's) to the valence bands (VB's). Neglect of the CB-VB interactions decouples the Hamiltonian into a 2×2 CB block and a 6×6 VB block, both of which depend explicitly on strain and wave vector. The CB block is solved directly, whereas the VB block is further simplified to two 3×3 blocks via a unitary transformation. A finite-element approach is finally used to solve the resulting sets of coupled differential equations directly to obtain eigenfunctions and eigenvalues at each in-plane wave vector $k_\parallel$ of interest. Interband matrix elements are then obtained for various $k_\parallel$ directly from the normalized conduction and valence subband eigenfunctions.

The modified superlattice $\mathbf{K}\cdot\mathbf{p}$ approach we use to treat strained-layer superlattices utilizes the envelope-function scheme in a somewhat different way. (Here $\mathbf{K}$ denotes the wave vector describing the superlattice Bloch states, which replaces the bulk wave vector $\mathbf{k}$ as a useful quantum number in the presence of the superlattice potential.) Strain-dependent envelope functions for superlattice subband states at $\mathbf{K}=\mathbf{0}$ are obtained in closed form by suitably simplifying the general 8×8 Hamiltonian matrix and treating strain effects in the quantum well and barrier layers perturbatively. This allows for evaluation of momentum matrix elements between superlattice subband states at $\mathbf{K}=\mathbf{0}$, which, with energies of these superlattice zone-center states obtained using a modified Kronig-Penney model, facilitates solution of a superlattice $\mathbf{K}\cdot\mathbf{p}$ equation for eigenenergies of states with finite $\mathbf{K}$. Eigenfunctions and interband matrix elements for $\mathbf{K}\neq\mathbf{0}$ are then obtained numerically. The two models will now be described in further detail.

B. Finite-element model for quantum wells

In constructing the Hamiltonian matrix for treating the strained SQW's, we use the Luttinger-Kohn form for the $\mathbf{k}\cdot\mathbf{p}$ interactions[7,8] and the Pikus-Bir Hamiltonian[9] for treating energy shifts and interband interactions due to strain. Neglecting interactions between conduction and valence bands, the resulting 8×8 matrix decouples into a simple diagonal 2×2 conduction-band matrix and a 6×6 valence-band matrix of the form

$$\mathbf{H}_{\mathrm{VB}}(\mathbf{k})=\begin{bmatrix} a_+ & b & i/\sqrt{2}b & -i\sqrt{2}c & c & 0 \\ b^* & a_- & if & i\sqrt{\frac{3}{2}}b & 0 & c \\ -i/\sqrt{2}b^* & -if^* & d & 0 & i\sqrt{\frac{3}{2}}b & i\sqrt{2}c \\ i\sqrt{2}c^* & -i\sqrt{\frac{3}{2}}b^* & 0 & d & -if^* & i/\sqrt{2}b \\ c^* & 0 & -i\sqrt{\frac{3}{2}}b^* & if & a_- & -b \\ 0 & c^* & -i\sqrt{2}c^* & -i/\sqrt{2}b^* & -b^* & a_+ \end{bmatrix}, \tag{10}$$

where

$$a_+=-\frac{\hbar^2}{2m_0}[(\gamma_1+\gamma_2)(k_x^2+k_y^2)+(\gamma_1-2\gamma_2)k_z^2]+V_{\mathrm{hh}}\ , \tag{11}$$

$$a_-=-\frac{\hbar^2}{2m_0}[(\gamma_1-\gamma_2)(k_x^2+k_y^2)+(\gamma_1+2\gamma_2)k_z^2]+V_{\mathrm{lh}}\ , \tag{12}$$

$$b=i\sqrt{3}\frac{\hbar^2}{m_0}\gamma_3 k_z(k_x-ik_y)\ , \tag{13}$$

$$c=-\frac{\sqrt{3}}{2}\frac{\hbar^2}{m_0}[(k_x^2-k_y^2)\gamma_2-2ik_xk_y\gamma_3]\ , \tag{14}$$

$$d=-\frac{\hbar^2}{2m_0}\gamma_1(k_x^2+k_y^2+k_z^2)+Aa_v\varepsilon-\Delta+V_{\mathrm{so}}\ , \tag{15}$$

$$f=\sqrt{2}\frac{\hbar^2}{2m_0}[\gamma_2(k_x^2+k_y^2-2k_z^2)]-\frac{\sqrt{2}}{3}Bb_v\varepsilon\ . \tag{16}$$

Here $|\mathbf{k}|^2=k^2=k_x^2+k_y^2+k_z^2$, $\hbar$ is the reduced Planck's constant, m_0 is the free-electron mass, γ_1, γ_2, and γ_3 are the Luttinger parameters, and a_v and b_v are the hydrostatic and uniaxial valence-band deformation potentials. A and B are parameters defined in terms of the elastic constants C_{11} and C_{12} as

$$A=2\left[\frac{C_{11}-C_{12}}{C_{11}}\right], \tag{17}$$

$$B=3\left[\frac{C_{11}+2C_{12}}{C_{11}}\right], \tag{18}$$

and ε is the strain

$$\varepsilon=\frac{a_{\parallel}-a}{a}\ , \tag{19}$$

where $a_{\parallel}$ is the in-plane lattice constant of the strained layer and a is the unstrained lattice constant. V_{hh} and V_{lh} correspond to the strain-dependent energies of the heavy-hole and light-hole valence-band edges, respectively, and V_{so} is the energy of the split-off band edge absent strain and spin-orbit interactions (i.e., the unstrained values of V_{hh} and V_{lh}). These energies will obviously differ for matrices describing the quantum well and barrier layers. Note that the VB basis functions were ordered as $|\frac{3}{2},+\frac{3}{2}\rangle$, $|\frac{3}{2},+\frac{1}{2}\rangle$, $|\frac{1}{2},-\frac{1}{2}\rangle$, $|\frac{1}{2},-\frac{1}{2}\rangle$, $|\frac{3}{2},-\frac{1}{2}\rangle$, and $|\frac{3}{2},-\frac{3}{2}\rangle$ in generating the Hamiltonian matrix given above.

Applying the unitary transformation described in Appendix A, the valence-band Hamiltonian matrix transforms to a block diagonal form. With the axial approximation (i.e., $\gamma_2,\gamma_3\rightarrow\gamma$ in Eq. (14) with $\gamma\equiv[\gamma_2+\gamma_3]/2$), the upper and lower 3×3 blocks of this matrix take the form

$$\mathbf{H}_{\mathrm{VB}}(k_{\parallel},k_z)=\begin{bmatrix} A_+ & C\mp iB & \sqrt{2}C\pm\frac{iB}{\sqrt{2}} \\ C\pm iB & A_- & F\mp i\sqrt{\frac{3}{2}}B \\ \sqrt{2}C\mp\frac{iB}{\sqrt{2}} & F\pm i\sqrt{\frac{3}{2}}B & D \end{bmatrix} \tag{20}$$

with

$$A_+=-\frac{\hbar^2}{2m_0}[(\gamma_1+\gamma_2)k_{\parallel}^2+(\gamma_1-2\gamma_2)k_z^2]+V_{\mathrm{hh}}\ , \tag{21}$$

$$A_-=\frac{\hbar^2}{2m_0}[(\gamma_1-\gamma_2)k_{\parallel}^2+(\gamma_1+2\gamma_2)k_z^2]+V_{\mathrm{lh}}\ , \tag{22}$$

$$B=\sqrt{3}\frac{\hbar^2}{m_0}\gamma_3 k_z k_{\parallel}\ , \tag{23}$$

$$C=\frac{\sqrt{3}}{2}\frac{\hbar^2}{m_0}\gamma k_{\parallel}^2\ , \tag{24}$$

$$D=-\frac{\hbar^2}{2m_0}\gamma_1(k_{\parallel}^2+k_z^2)+Aa_v\varepsilon-\Delta+V_{\mathrm{so}}\ , \tag{25}$$

$$F=-\sqrt{2}\frac{\hbar^2}{2m_0}\gamma_2(k_{\parallel}^2-2k_z^2)-\frac{\sqrt{2}}{3}Bb_v\varepsilon\ . \tag{26}$$

The upper and lower signs appearing in the off-diagonal terms correspond to the upper and lower blocks, respectively, and $k_{\parallel}$ is the magnitude of the in-plane wave vector. Making the usual substitution $k_z\rightarrow-i(\partial/\partial z)$ results in two 3×3 matrix operators from which the valence-band dispersions can be obtained given appropriate boundary conditions. The eigenvalue equation for each block is of the form

$$\mathbf{H}_{\mathrm{VB}}\left[k_{\parallel},-i\frac{\partial}{\partial z}\right]\psi=E_{\mathrm{VB}}(k_{\parallel})\psi\ . \tag{27}$$

Conduction-band energies are simply the eigenvalues of

the operator

$$\mathbf{H}_{\mathrm{CB}}(k_{\parallel})=-\frac{\hbar^2}{2m_e^*}\frac{\partial^2}{\partial z^2}+\frac{\hbar^2 k_{\parallel}^2}{2m_e^*}+V_c \ , \tag{28}$$

where m_e^* is the electron effective mass and V_c is the strain-dependent conduction-band edge energy.

Explicit solution of Eqs. (27) and (28) requires knowledge of the energy-band offsets. In this work, we obtain the strain splitting of the energies V_{hh} and V_{lh} in the quantum-well layer and their values relative to the degenerate valence-band edge in the unstrained barriers using strain-dependent tight-binding heterojunction offset calculations.[10] Deformation potentials a_v and b_v are then obtained which would lead to these same band energies through degenerate perturbation theory based on the Pikus-Bir Hamiltonian. (The values of a_v and b_v obtained in this manner, which are close to experimental values, are used throughout for consistency.) This allows us to then use perturbation theory to obtain V_c and V_{so} from the tight-binding values of V_{hh} and V_{lh}. Using this procedure, V_{hh}, V_{lh}, V_{so}, and V_c can be obtained for the strained quantum well and unstrained barrier layers, and sets of differential equations can be obtained via Eqs. (27) and (28) for each region. These equations can then be solved for the dispersions given boundary conditions, which are obtained by integration across the interfaces.[11] Note that for the case of flat-band heterostructures considered here, the sets of eigenvalues resulting from solution of the upper and lower 3×3 valence-band blocks are identical.

In order to solve the sets of coupled differential equations describing the valence bands, we use a finite-element analysis. In this approach, which has previously been applied by Nakamura *et al.*[12] to the single-band problem, the problem space is subdivided along the z axis into finite elements of equal length. We follow Nakamura's procedure in obtaining conduction-band eigenfunctions and eigenvalues, and treat the valence bands as follows: A basis set consisting of four third-order Hermitian line elements is used to describe each valence-band state within each finite element. Application of the standard Galerkin procedure to Eq. (27) yields a 12×12 matrix for each of the two 3×3 Hamiltonian matrix blocks within each finite element. This yields discretized equations for each finite element of the form $[A]_e[\psi]_e=E(k)[M]_e[\psi]_e$, where $[A]_e$ and $[M]_e$ are matrices specified by the Galerkin procedure and $[\psi]_e$ is the wave-vector contribution for the finite element under consideration. Boundary conditions are applied by forming transfer matrices $[T]$ at each interface between different materials, and transforming the right-hand-side finite element as $[A]_e=[T]^T[A]_e[T]$ and $[M]_e=[T]^T[M]_e[T]$. A global matrix is then obtained by adding the contributing finite-element matrices together, resulting in a generalized eigenvalue problem of the form $[A][\psi(k)]=E(k)[M][\psi(k)]$. Here $[A]$ and $[M]$ are obtained from the addition of the individual finite-element matrices $[A]_e$ and $[M]_e$ and $[\psi(k)]$ is the eigenfunction corresponding to the eigenvalue $E(k)$. This global equation is generated and solved for each in-plane k value of interest, resulting in the full valence dispersion. The eigensolver uses a k-step Arnoldi update algorithm[13] and allows us to take advantage of the sparse and banded structure of the $[A]$ and $[M]$ matrices.

To obtain optical matrix elements, the wave functions obtained from the finite-element solution are first normalized for the qth valence state and the pth conduction state by requiring

$$|\psi_q|^2=|\psi_q^{\mathrm{hh}}|^2+|\psi_q^{\mathrm{lh}}|^2+|\psi_q^{\mathrm{so}}|^2=1 \tag{29}$$

and

$$|\phi_p|^2=1 \ ,$$

where ψ_q is the qth valence-subband envelope function, ψ_q^{hh}, ψ_q^{lh}, and ψ_q^{so} are the heavy-hole, light-hole, and split-off band envelope-function contributions to ψ_q, respectively, and ϕ_p is the pth conduction-band envelope function. The matrix element for optical transitions between the pth conduction and qth valence eigenstates is given by

$$M_{pq}^{\alpha}(k_{\parallel})=\sum_n \langle \psi_q|\phi_p\rangle\langle n|\mathbf{e}\cdot\mathbf{p}|S,\alpha\rangle \ , \tag{30}$$

where $k_{\parallel}$ is the in-plane k-vector magnitude, $|n\rangle$ is the nth transformed Bloch function from Appendix A, $\mathbf{e}$ is the polarization vector, $\mathbf{p}$ is the momentum operator, and α is the conduction spin state ($\alpha=\uparrow$ or $\downarrow$). Final squared matrix elements are obtained by squaring the above equation and averaging over the x-y plane, which eliminates all the cross-coupling terms.

C. $\mathbf{K}\cdot\mathbf{p}$ model for superlattices

In this work, superlattice structures are treated using a superlattice $\mathbf{K}\cdot\mathbf{p}$ theory[14,15] modified to include strain effects. Dispersions are obtained by solving a $\mathbf{K}\cdot\mathbf{p}$ equation obtained using superlattice Bloch functions

$$|L,\mathbf{K}\rangle=U_{L,\mathbf{K}}(\mathbf{r})\exp(i\mathbf{K}\cdot\mathbf{r}) \ , \tag{31}$$

where L is the superlattice subband index, $U_{L,\mathbf{K}}(\mathbf{r})$ has the periodicity of the superlattice potential, and $\mathbf{K}=\mathbf{K}_{\perp}+\mathbf{K}_{\parallel}$ is the superlattice wave vector with the $\parallel$ and $\perp$ components parallel and normal to the layer plane, respectively. Expanding $U_{L,\mathbf{K}}(\mathbf{r})$ in a basis of zone-center subband states $|N',0\rangle$ as

$$U_{L,\mathbf{K}}(\mathbf{r})=\sum_{N'=1}^{N'_{\max}} c_{L,N'}(\mathbf{K})|N',0\rangle \ , \tag{32}$$

substituting into the time-independent Schrodinger equation, and multiplying from the left by $\langle N,0|$ yields the superlattice $\mathbf{K}\cdot\mathbf{p}$ equation

$$\sum_{N'=1}^{N'_{\max}} c_{L,N'}(\mathbf{K})\left\{\left[E_N(0)-E_L(\mathbf{K})+\frac{\hbar^2}{2m_0}|\mathbf{K}|^2\right]\delta_{N,N'}+\frac{\hbar}{m_0}\mathbf{K}\cdot P_{N,N'}\right\}=0 \tag{33}$$

where

$$P_{N,N'}=\langle N,0|\mathbf{p}|N',0\rangle \ . \tag{34}$$

Further describing the superlattice zone-center subband

states in terms of zone-center bulk states in an envelope-function expansion

$$|N,0\rangle=\sum_{\nu=1}^{\nu_{\max}} F_{\nu,|N,0\rangle}(\mathbf{r})|\nu,0\rangle \tag{35}$$

and assuming that the spatial variation of the functions $F_{\nu,|N,0\rangle}$ is much slower than that of the bulk cell-periodic functions $u_\nu(\mathbf{r})$, the superlattice momentum matrix elements at $\mathbf{K}=\mathbf{0}$ become simply

$$P_{N,N'}=\sum_{\nu=1}^{\nu_{\max}}\sum_{\nu'=1}^{\nu_{\max}}\langle F_{\nu,|N,0\rangle}|F_{\nu',|N',0\rangle}\rangle p_{\nu,\nu'} , \tag{36}$$

where $p_{\nu,\nu'}$ are well-known bulk zone-center matrix elements

$$p_{\nu,\nu'}=\langle u_\nu(\mathbf{r})|\mathbf{p}|u_{\nu'}(\mathbf{r})\rangle . \tag{37}$$

We use this formalism to obtain strained-layer superlattice subbands and matrix elements as follows. We first construct Hamiltonian matrices valid for $\mathbf{K}=\mathbf{0}$ in the *absence* of strain using the envelope-function approach. Specifically, we generate matrices for the quantum-well and barrier materials at $\mathbf{k}_\parallel=\mathbf{0}$, ordering the bulk basis functions as $|\frac{1}{2},+\frac{1}{2}\rangle_c$, $|\frac{3}{2},+\frac{3}{2}\rangle$, $|\frac{3}{2},+\frac{1}{2}\rangle$, $|\frac{1}{2},+\frac{1}{2}\rangle$, $|\frac{1}{2},-\frac{1}{2}\rangle_c$, $|\frac{3}{2},-\frac{3}{2}\rangle$, $|\frac{3}{2},-\frac{1}{2}\rangle$, and $|\frac{1}{2},-\frac{1}{2}\rangle$. Using the Luttinger-Kohn form for the $\mathbf{k}\cdot\mathbf{p}$ interactions, and following Johnson *et al.*[14] in neglecting terms coupling $|M_J|=\frac{1}{2}$ states which account for interactions with bands not in the basis set, a block-diagonal 8×8 matrix results which consists of an upper left 4×4 matrix for $+M_J$ states and a similar lower right 4×4 matrix for $-M_J$ states. Next, we use the Pikus-Bir strain Hamiltonian and the same ordering of the bulk basis functions to generate a strain matrix. While this matrix can be added directly to the unstrained matrix to obtain a net Hamiltonian appropriate for the strained layer, such a procedure yields an 8×8 matrix which cannot be solved analytically for the envelope functions $F_{\nu,|N,0\rangle}$. We thus include the strain matrix using a form of perturbation theory cast as a unitary transformation,[16] which yields a block diagonal 8×8 Hamiltonian from which it is possible to obtain analytical forms for the envelope functions at the superlattice zone center.

The upper-left $+M_J$ block of this matrix is of the form

$$\mathbf{H}_+(k_z)=\begin{bmatrix} H_{11} & 0 & H_{31}^* & H_{41}^* \\ 0 & H_{22} & 0 & 0 \\ H_{31} & 0 & H_{33} & 0 \\ H_{41} & 0 & 0 & H_{44} \end{bmatrix} , \tag{38}$$

where

$$H_{11}=V_c=Aa_c\varepsilon , \tag{39}$$

$$H_{31}=-\sqrt{\tfrac{2}{3}}P\hbar k_z , \tag{40}$$

$$H_{41}=-\sqrt{\tfrac{1}{3}}P\hbar k_z , \tag{41}$$

$$H_{22}=V_{\rm hh}-\frac{\hbar^2k_z^2}{2m_{\rm hh}}+Aa_v\varepsilon+\frac{Bb_v\varepsilon}{3} , \tag{42}$$

$$H_{33}=V_{\rm lh}+Aa_v\varepsilon-\frac{Bb_v\varepsilon}{3}-\frac{\left[\dfrac{\sqrt{2}Bb_v\varepsilon}{3}+\dfrac{\varepsilon\Delta}{9\sqrt{2}}\right]^2}{\dfrac{Bb_v\varepsilon}{3}+\Delta} , \tag{43}$$

$$H_{44}=-\Delta+V_{\rm so}+Aa_v\varepsilon+\frac{\left[\dfrac{\sqrt{2}Bb_v\varepsilon}{3}+\dfrac{\varepsilon\Delta}{9\sqrt{2}}\right]^2}{\dfrac{Bb_v\varepsilon}{3}+\Delta} . \tag{44}$$

Here V_c, $V_{\rm hh}$, $V_{\rm lh}$, and $V_{\rm so}$ are the energies of the various band edges in the absence of strain. These energies are determined for the various layers from unstrained band gaps and strain-dependent tight-binding valence-band offsets[10] via the Pikus-Bir strain Hamiltonian[9] in a manner similar to that described in Sec. III A. With these energies and appropriate boundary conditions,[11] the superlattice zone-center envelope functions are obtained in closed form from Eqs. (38)–(44) and their matrix elements are obtained from Eq. (36). (These functions are tabulated in Appendix B.) The energies for these superlattice subband states at $\mathbf{K}=\mathbf{0}$ are obtained using a modified Kronig-Penney model.[17]

Superlattice subband dispersions and eigenfunctions are finally obtained by substituting the zone-center energies and matrix elements into the superlattice $\mathbf{K}\cdot\mathbf{p}$ equation [Eq. (33)] and solving this equation numerically. Interband matrix elements between superlattice subband states are then obtained as products of superlattice zone-center matrix elements and overlap integrals between envelope functions for the subband states as in Refs. 14 and 15. We have used a thirty-six subband superlattice $\mathbf{K}\cdot\mathbf{p}$ expansion in our calculations [i.e., $N'_{\max}=36$ in Eq. (33)], and have confirmed that such an expansion is sufficiently large for accurate calculation of the near-gap dispersion relations in the types of superlattices studied here. For the superlattice structures examined in this work (cf. Sec. III B), reduction of the basis set to twenty-four subbands changes calculated eigenenergies by only a meV or so over the entire ranges of energies and wave vectors we have studied. We thus conclude that, for the superlattices of interest in this work, our $\mathbf{K}\cdot\mathbf{p}$ expansion is sufficiently complete for accurate numerical calculations of near-gap electronic structure.

D. Comparison of approaches

All of the calculations which follow in Sec. III use the finite-element model for isolated quantum wells and the superlattice $\mathbf{K}\cdot\mathbf{p}$ model for multilayer SLS's. While this is appropriate for reasons of computational simplicity, it is useful to compare the results from both models where possible in order to ensure that qualitative features of the calculated band structures are not artifacts of the models themselves. While somewhat different results can be expected from the two very different approaches, owing to differences in both the formalism and implementation, band structures from the two models should be similar when applied to identical structures. Such comparisons can be made by comparing results for an isolated quan-

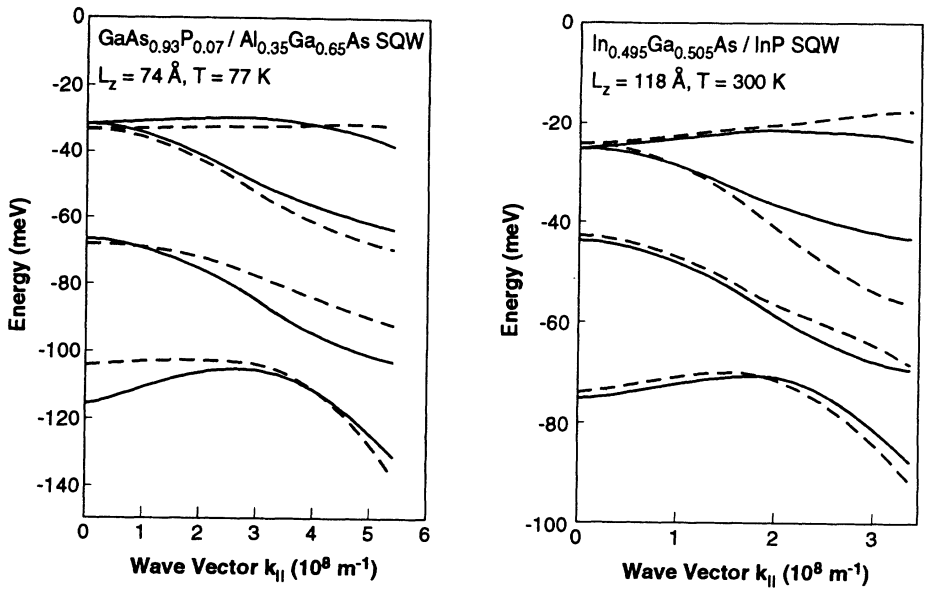

FIG. 1. In-plane energy band structures for isolated $GaAs_{0.93}P_{0.07}/Al_{0.35}Ga_{0.65}As$ and $In_{0.495}Ga_{0.505}As/InP$ quantum wells obtained using the finite-element (solid) and superlattice $\mathbf{K}\cdot\mathbf{p}$ (dashed) models described in this work. Dispersions calculated from the two very different techniques are generally in excellent agreement near the zone center, but deviate somewhat at large finite $k_{\|}$ owing to differences in assumptions made regarding interband interactions.

tum well obtained from the finite-element model to those from the $\mathbf{K}\cdot\mathbf{p}$ model for a thick-barrier superlattice with similar quantum-well widths and quantum-well and barrier compositions.

We have carried out such comparison studies, choosing to examine structures in the $GaAs_{1-x}P_x/Al_xGa_{1-x}As$ and $In_xGa_{1-x}As/InP$ system where the light- and heavy-hole valence-band energies are similar at $k_{\|}=0$. These are meaningful *and rather stringent* test cases since interactions between the various valence bands are strongest when the bands are in close proximity energetically. Calculated in-plane energy-band structures for isolated $GaAs_{0.93}P_{0.07}/Al_{0.35}Ga_{65}As$ and $In_{0.495}Ga_{0.505}As/InP$ quantum wells with merged valence-band edges at $k_{\|}=0$ are shown in Fig. 1. Solid curves represent results from the finite-element model, whereas results from the superlattice $\mathbf{K}\cdot\mathbf{p}$ calculations are indicated by dashed curves. Numerical values for material parameters used to obtain these results and all other results in this work are tabulated in Appendix C. Note that energies and band shapes calculated from the two techniques are generally in excellent agreement near the zone center. Deviations between results from the two models become evident at large finite $k_{\|}$, but the overall qualitative shapes of the bands calculated using the two very different approaches are remarkably similar for both material systems. Differences in the band shapes may result primarily from differences in approximations made regarding band coupling in the two models, whereas the small discrepancies in the zone-center subband energies result from different treatments of effective masses in the two models. Literature values are used for all masses in the finite-element approach, but are used only for the heavy-hole masses in the superlattice $\mathbf{K}\cdot\mathbf{p}$ model with the other masses interrelated through Kane matrix elements. The two models will now be applied to the study of a variety of structures utilizing tensile-strain effects.

III. RESULTS AND DISCUSSION

A. Tensile-strained quantum wells

In this section, the finite-element model described above is applied to the calculation of in-plane valence-band dispersion relations and interband optical matrix elements in isolated tensile-strained quantum wells. $GaAs_{1-x}P_x/Al_{0.35}Ga_{0.65}As$ and $In_xGa_{1-x}As/InP$ structures with all strain confined to the quantum wells, which could be grown directly on GaAs and InP substrates, respectively, are examined. Before examining dispersions for particular structures, however, we present calculated composition and well-width dependences of the fundamental e-lh and e-hh interband optical transition energies in Figs. 2 and 3.

In Fig. 2, transition energies at 77 K are shown for the $GaAs_{1-x}P_x/Al_{0.35}Ga_{0.65}As$ system as a function of quantum-well width for different compositions. Thin solid curves represent fundamental e-hh transitions and dashed curves represent e-lh transitions. The bold solid curve represents combinations of well widths and compositions which result in merging of the uppermost light- and heavy-hole valence-band edges, and thus delineates the boundary between regimes yielding light-hole-up and heavy-hole-up valence-subband configurations. Note that the quantum wells are under tensile strain for all compositions in this system, and that merging of the e-lh and e-hh transition energies is achieved in sufficiently narrow quantum-well widths. Similar results are shown for the $In_xGa_{1-x}As/InP$ system in Fig. 3, with fundamental e-hh and e-lh transition energies again denoted by thin solid and dashed curves, respectively, and the merger point denoted by the bold solid curve. The primary qualitative difference between these results and those of Fig. 2 is that quantum wells with both compressive ($x>0.53$) and tensile ($x<0.53$) strain are represented here. Note that merging of the e-lh and e-hh transition energies is

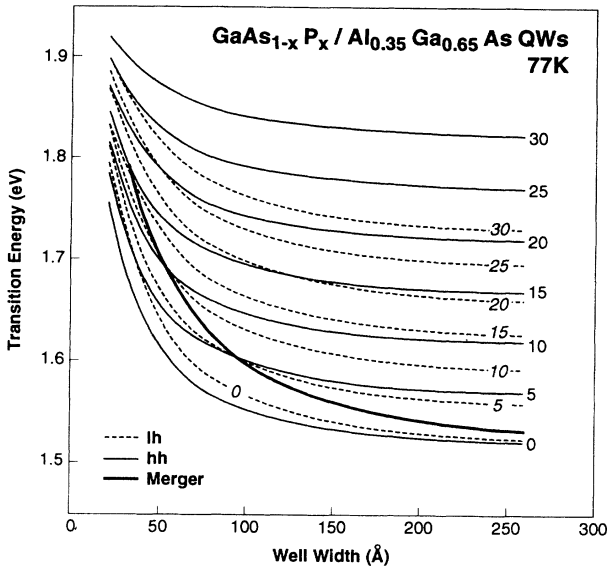

FIG. 2. Calculated optical transition energies as a function of well width for isolated $GaAs_{1-x}P_x/Al_{0.35}Ga_{0.65}As$ quantum wells of various compositions. Solid curves represent fundamental e-hh transitions and dashed curves represent e-lh transitions. Numerical labels on the curves denote percentage of GaP in the $GaAs_{1-x}P_x$ quantum wells. The bold solid curve indicates the combination of compositions and well widths that yield merging of the uppermost light- and heavy-hole subbands at the zone center. The quantum wells are under tensile strain for all compositions, and the barriers are assumed unstrained.

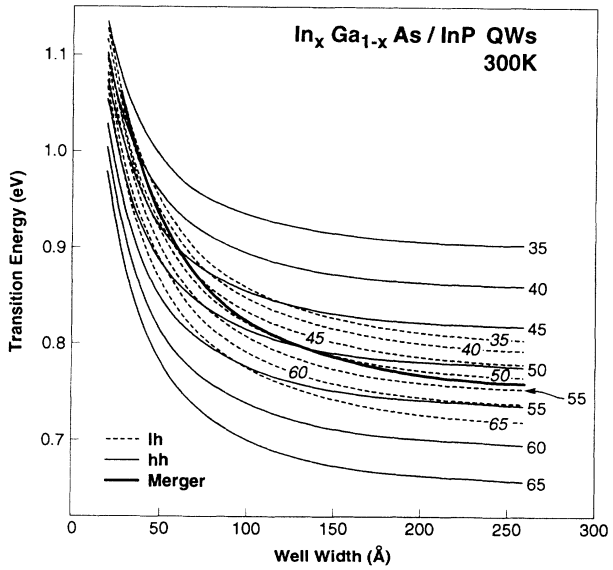

FIG. 3. Calculated optical transition energies as a function of well width for isolated $In_xGa_{1-x}As/InP$ quantum wells of various compositions. Fundamental e-hh (solid) and e-lh (dashed) transitions are represented, with merging of the two transition energies represented by the bold solid curve as in Fig. 2. Numerical labels on the curves denote the percentage of InAs in the $In_xGa_{1-x}As$ quantum wells. The InP barriers are assumed to be unstrained, whereas the quantum wells are under compressive strain for $x > 0.53$ and tensile strain for $x < 0.53$.

again achieved in sufficiently narrow quantum wells with tensile strain but is impossible in the compressively strained structures. While most of the quantum wells represented in these figures are of thicknesses below critical values for dislocation formation, the thicker wells with compositions greater than $x \geq 25\%$ in Fig. 2 and $x \leq 40\%$ in Fig. 3 approach or just exceed these values.

Figures 2 and 3 illustrate band gaps and valence-subband ordering over relatively wide ranges of quantum-well widths and compositions. We focus now on structures with well widths and compositions yielding merged or nearly merged valence-subband edges, i.e., samples lying near the bold solid contours in Figs. 2 and 3. Relatively small differences in quantum-well compositions or thicknesses can clearly change the ordering of the uppermost light- and heavy-hole valence subbands in this regime. Because of the strong interactions between the various valence-band states, these small differences in the physical structure are accompanied by significant modifications in the band structure and optical properties near the band edge in these structures. We now demonstrate this through studies of "composition tuning" and "well-width tuning" of the valence-band configuration through the merger point in both $GaAs_{1-x}P_x/Al_xGa_{1-x}As$ and $In_xGa_{1-x}As/InP$ tensile-strained quantum-well structures and examine the consequences for band structures and optical matrix elements.

Calculated energy-band structures and $k_{\|}$-dependent squared optical matrix elements for 65 Å $GaAs_{1-x}P_x/Al_{0.35}Ga_{0.65}As$ quantum wells of three different compositions are shown in Fig. 4. The wave vector $k_{\|}$ again lies in the plane of the layer, and matrix elements are shown for interband transitions involving the uppermost heavy- and light-hole subbands for light polarized both within the plane of the layer (TE) and perpendicular to this plane (TM). Solid and dashed curves represent heavy- and light-hole dispersions in the band-structure diagrams, respectively. Similarly, e-hh and e-lh optical transitions are represented by solid and dashed lines, respectively, in the plots of the $k_{\|}$-dependent matrix elements, with TM matrix elements represented by bold curves and TE elements represented by thin curves. Subband energies are referenced to the uppermost edge of the valence-band potential well, and the squared matrix elements are in units of $|\mathbf{P}|^2 = |\langle V,\alpha|\mathbf{p}|S,\alpha\rangle|^2$. (Here V is any one of the functions X, Y, or Z defined in Sec. II A and again $\alpha = \uparrow$ or $\downarrow$.) These conventions will be used throughout the remainder of this paper.

The "nominal" quantum well (center) in Fig. 4 with $x = 0.080$ exhibits a merged valence-band configuration, whereas the other two have been rendered heavy-hole-up by 5 meV (left, $x = 0.065$) and light-hole-up by 5 meV (right, $x = 0.095$) by composition tuning. Note the significant changes in the shapes of the uppermost valence bands near the zone center, including inversion of the sign of the hole effective masses for both the heavy- and light-hole subbands as they are tuned through the merger point.[18] Note also the drastic changes in the $k_{\|}$-dependent interband matrix elements which accompany the relatively small changes in the valence-subband ener-

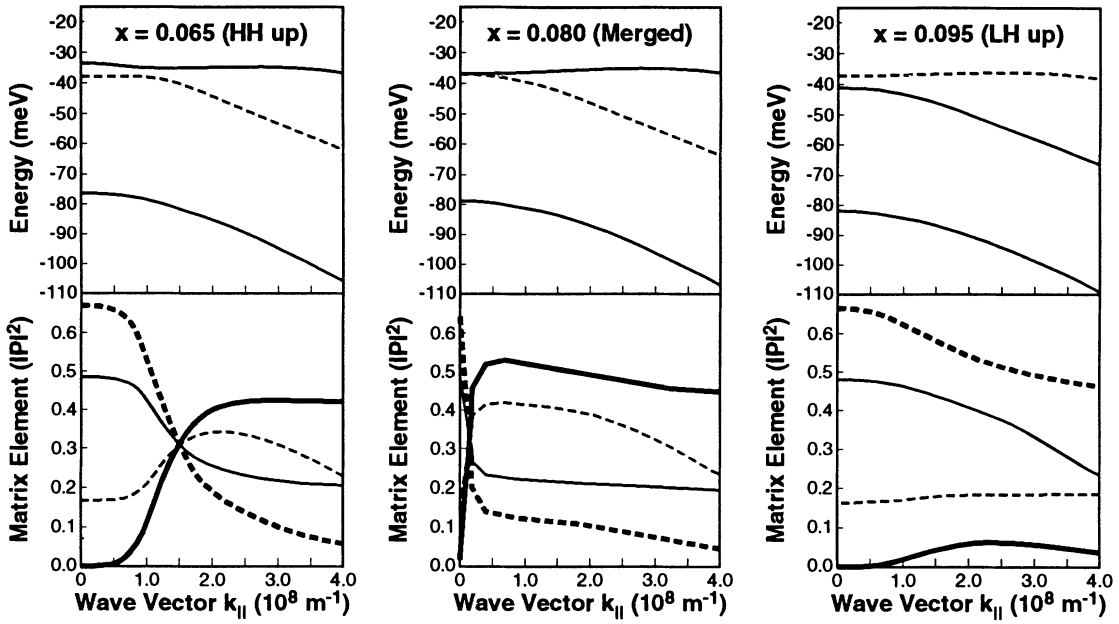

FIG. 4. In-plane energy band structures and $k_{\|}$-dependent optical matrix elements (TE and TM) for 65 Å $GaAs_{1-x}P_x/Al_{0.35}Ga_{0.65}As$ quantum wells of various compositions near the band merger point. Dispersions are shown for structures that are heavy-hole up by 5 meV, merged, and light-hole up by 5 meV, with heavy- and light-hole subbands denoted by solid and dashed curves, respectively. TE and TM matrix elements for interband transitions involving the uppermost valence subbands are denoted by thin and bold curves, respectively, with solid curves representing e-hh matrix elements and dashed curves e-lh elements. Note that the band shapes and matrix elements fluctuate significantly with small changes in composition due to the strong coupling between the valence bands near the merger point.

gies. Two features of the matrix elements are particularly significant: First, all four interband matrix elements differ significantly from their zone-center values over a range of only 0.5×10^{-8} m ($\sim1\%$ of $\pi/a_{\|}$ with $a_{\|}=5.653$ Å) in the merged case, suggesting that the common approximation of $k_{\|}$-independent matrix elements may be invalid for calculations of optical properties in these structures. Second, the electron–heavy-hole TM matrix element becomes strongly suppressed at finite $k_{\|}$ in the light-hole-up case. This is explained by examination of the wave functions. The TM e-hh transitions are allowed at finite $k_{\|}$ because of significant mixing of a light-hole component into the heavy-hole subband states. This light-hole component is, however, nearly orthogonal to the lowest conduction subband states in the light-hole-up case. This suppression, combined with the observed enhancement of the e-lh TM matrix elements in the same samples, may contribute significantly to the strong TM polarization of emission observed from tensile-strained lasers with light-hole-up valence-band configurations.[19] These calculations are for a lattice temperature of $T=77$ K.

In Fig. 5, a similar set of band structures with corresponding TE and TM optical matrix elements is shown which demonstrates well-width tuning through the merger point in $GaAs_{0.08}P_{0.92}/Al_{0.35}Ga_{0.65}As$ quantum wells. The nominal sample (center) is the same as that of Fig. 4, but here subband configurations which are heavy-hole up by 5 meV and light-hole up by 5 meV are obtained by changing the well widths to 55 and 80 Å, respectively, while keeping the composition constant. Note that tuning through the merger point by changing the well width produces variations in the band shapes and matrix elements which are significant and very similar to those obtained by composition tuning.

Analogous results of calculations showing composition and well-width tuning of the valence subbands through the merger point are shown for $In_xGa_{1-x}As/InP$ tensile-strained QW structures in Figs. 6 and 7, respectively. The valence-subband structure and corresponding optical matrix elements for a nominal $In_{0.49}Ga_{0.51}As/InP$ structure with $L_z=105$ Å is shown in the center of each figure. In Fig. 6, results are shown for structures in which subband configurations heavy-hole up and light-hole up by 5 meV have been obtained by varying the quantum-well composition about its nominal value. In Fig. 7, similar results are presented that demonstrate tuning of the subband structures by well-width variation to obtain 5 meV light-hole-up and heavy-hole-up valence-subband configurations. Significant changes in band shapes and matrix elements are again observed for both cases, with composition and well-width tuning yielding similar modifications. These results are similar to those obtained for the $GaAs_{1-x}P_x/Al_{0.35}Ga_{0.65}As$ system. (Apparent differences in the $k_{\|}$ dependence of the matrix elements at merging originate from choice of the uppermost valence-band type at $k_{\|}\neq0$.) A lattice temperature of 300 K was assumed for these calculations.

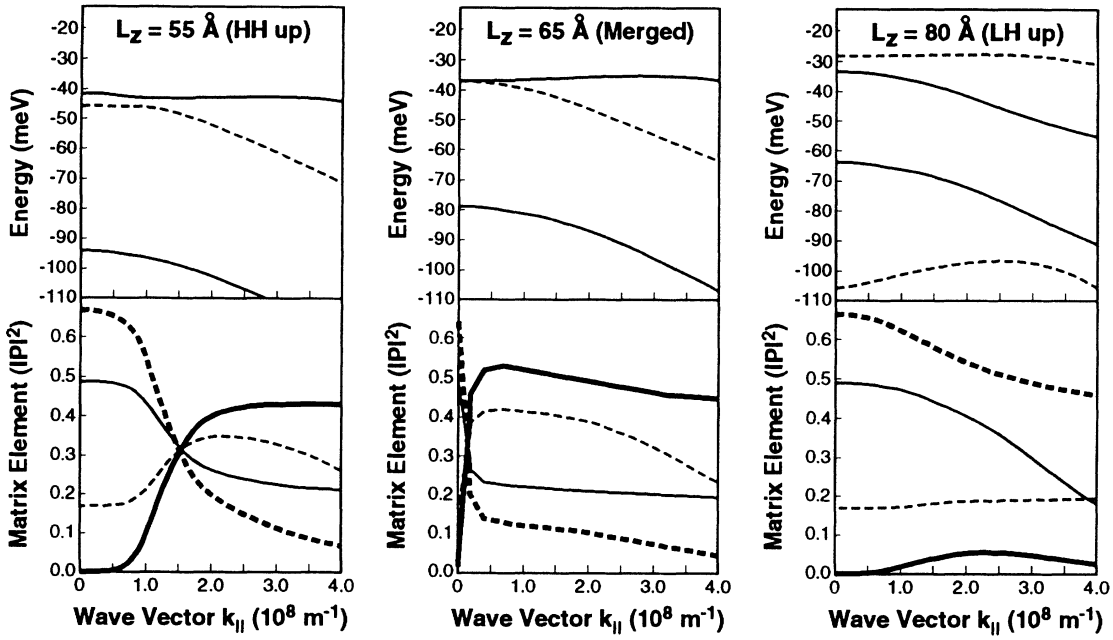

FIG. 5. In-plane energy band structures and $k_{\|}$-dependent optical matrix elements for $GaAs_{0.92}P_{0.08}/Al_{0.35}Ga_{0.65}As$ quantum wells of various thicknesses near the band merger point. Dispersions are again shown for structures that are heavy-hole up by 5 meV, merged, and light-hole up by 5 meV, and conventions are the same as those used in Fig. 4. Note that tuning through the merger point by changing the well width produces variations in the band shapes and matrix elements similar to those obtained by composition tuning (see Fig. 4).

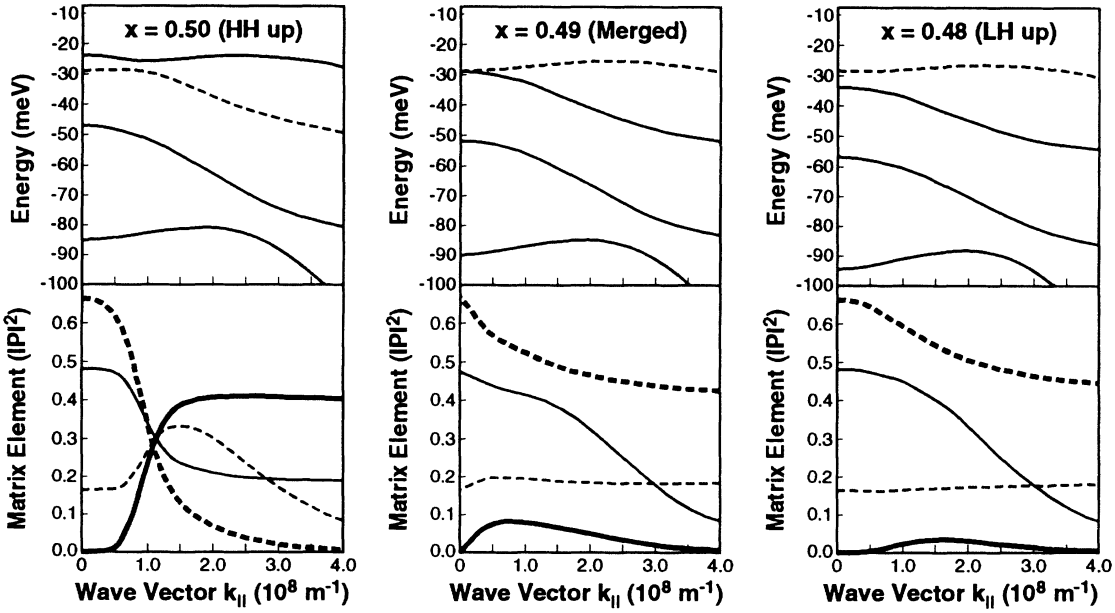

FIG. 6. In-plane energy band structures and $k_{\|}$-dependent optical matrix elements for 105 Å $In_xGa_{1-x}As/InP$ quantum wells of various compositions near the band merger point. Dispersions are shown for structures that are heavy-hole up by 5 meV, merged, and light-hole up by 5 meV, and conventions are the same as those used in Fig. 4.

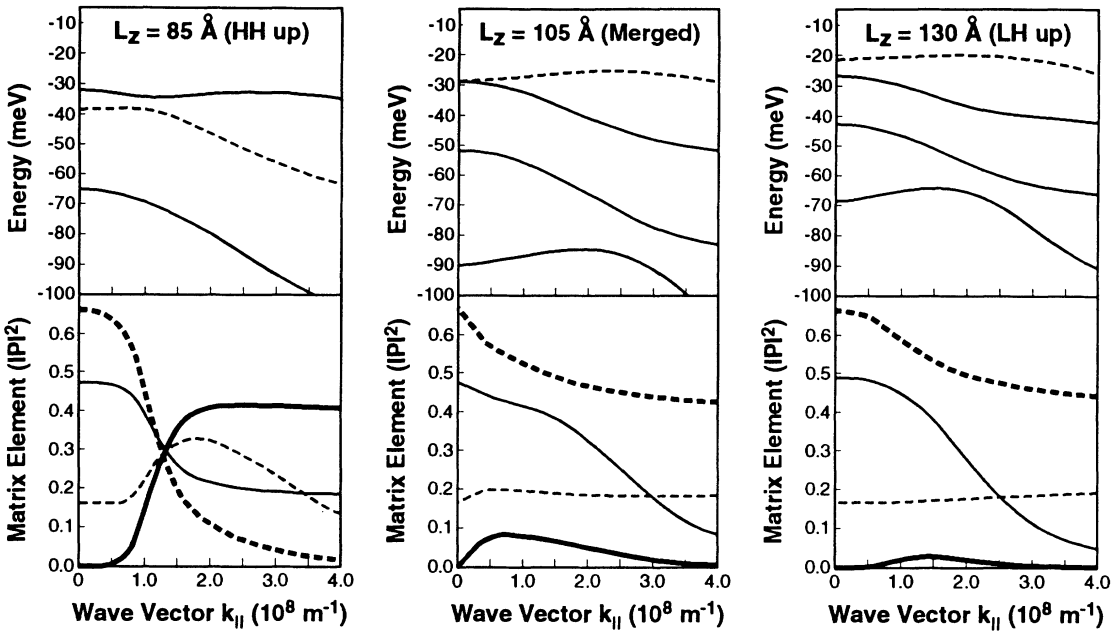

FIG. 7. In-plane energy band structures and $k_{\|}$-dependent optical matrix elements for $In_{0.49}Ga_{0.51}As/InP$ quantum wells of various thicknesses near the band merger point. Dispersions are again shown for structures that are heavy-hole up by 5 meV, merged, and light-hole up by 5 meV, and conventions are the same as those used in Fig. 4. The effects of well-width tuning of the valence-band structure are qualitatively similar to those obtained by composition tuning in this system (see Fig. 6).

B. Strained-layer superlattices

In this section, results are presented for superlattice $\mathbf{K}\cdot\mathbf{p}$ calculations of valence-band structures and optical matrix elements for $GaAs_{1-x}P_x/Al_yGa_{1-y}As$ and $In_xGa_{1-x}As/InP$ strained-layer superlattices (SLS's) involving tensile-strained component layers. We again focus on structures with merged or nearly merged uppermost light- and heavy-hole subbands, and specifically examine cases in which crossing of the uppermost valence subbands is induced by variation of barrier width alone. Band structures and squared optical matrix elements are calculated for wave vectors along directions parallel ($\mathbf{K}_{\|}=\mathbf{k}_{\|}$) and perpendicular ($\mathbf{K}_{\perp}$) to the layer planes, as both quantities are good quantum numbers in the periodic superlattice structures.

Energy band structures and squared optical matrix elements are shown in Fig. 8 for $GaAs_{0.90}P_{0.10}/Al_{0.35}Ga_{0.65}As$ strained-layer superlattices with 90 Å quantum wells and different barrier widths. The superlattices are assumed to be free-standing (or grown on graded buffers), with their in-plane lattice constants determined by balance of tensile strain in the $GaAs_{0.90}P_{0.10}$ wells and compressive strain in the $Al_{0.35}Ga_{0.65}As$ barriers. Variation of barrier width in such structures alters the distribution of strain between the well and barrier layers, the in-plane SLS lattice constant, and quantum-mechanical coupling between adjacent quantum-well layers. Large barrier widths favor a light-hole-up configuration through increased tensile strain in the quantum wells, although the increased quantum confinement in thick-barrier structures tends to reduce the strain splitting somewhat. The net effect in the structures of Fig. 8 is heavy-hole-up configuration for the thin barrier structures and a light-hole-up configuration for thick barrier structures. Specific cases are shown for which valence-subband configurations are heavy-hole up by 4 meV ($L_B=49$ Å), merged ($L_B=105$ Å), and light-hole up by 4 meV ($L_B=187$ Å) at the zone center, with tuning of the valence-band structure through the merger point again achieved entirely through variation of the barrier width. The matrix elements exhibit unusually sharp features at wave vectors for which interactions between the uppermost bands are strongest, but are otherwise qualitatively similar to those obtained for single quantum wells using the finite-element model. At finite in-plane wave vectors, tuning from a light-hole-up to a heavy-hole-up subband configuration tends generally to enhance the e-hh matrix elements and suppress the e-lh matrix elements for TE polarizations. The TM matrix elements follow the opposite trend.

In Fig. 9, valence band structures and matrix elements are shown for $In_{0.50}Ga_{0.50}As/InP$ strained-layer superlattices with tensile-strained 130 Å $In_{0.50}Ga_{0.50}As$ quantum wells and different InP barrier widths. (Wavelengths of photons resulting from the fundamental interband transition in these structures are in the 1.55-μm range important for optical communications.) In contrast to the SLS's of Fig. 8, these superlattices are assumed to be coherently strained to the substrates. All of the strain is thus confined to $In_{0.50}Ga_{0.50}As$ quantum wells, with the in-plane lattice constant fixed to that of the InP substrate, so changes in quantum-mechanical coupling are entirely responsible for changes in the subband structures resulting from variations in barrier widths. Cases are shown for which valence-subband configurations are heavy-hole up by $\sim$2 meV ($L_B=80$ Å), merged ($L_B=31$ Å), and light-hole up by $\sim$2 meV ($L_B=21$ Å). Note the substan-

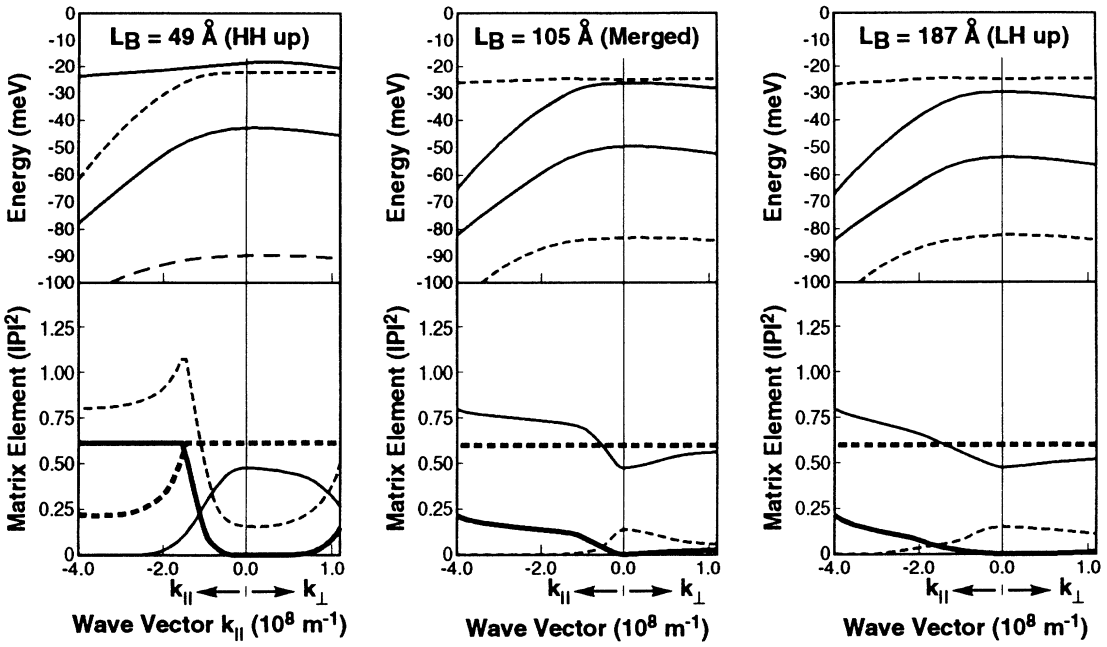

FIG. 8. Energy band structures and K-dependent optical matrix elements for $GaAs_{0.90}P_{0.10}/Al_{0.35}Ga_{0.65}As$ strained-layer superlattices with different barrier widths. The superlattices are assumed to be free-standing (or grown on graded buffers), with their in-plane lattice constants determined by balance of tensile strain in the $GaAs_{0.90}P_{0.10}$ wells and compressive strain in the $Al_{0.35}Ga_{0.65}As$ barriers. Cases are shown for which valence-subband configurations are heavy-hole up by 4 meV, merged, and light-hole up by 4 meV. Conventions are the same as those used in Fig. 4.

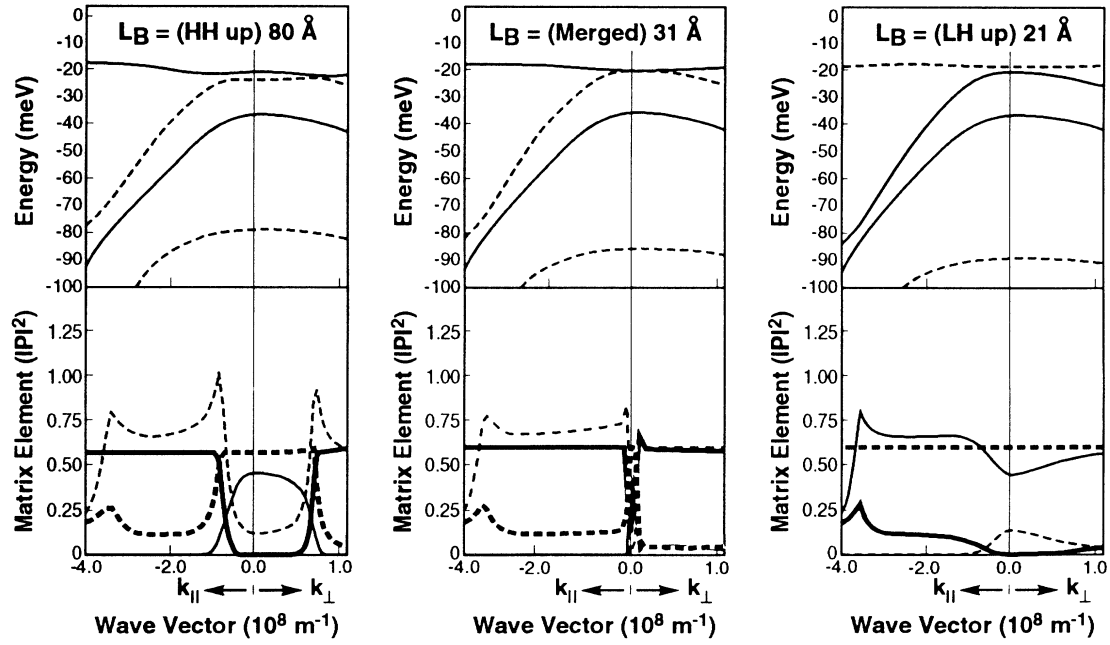

FIG. 9. Energy band structures and K-dependent optical matrix elements for $In_{0.50}Ga_{0.50}As/InP$ strained-layer superlattices with different widths. The superlattices are assumed to be coherently strained to InP substrates, with all of the strain confined to $In_{0.50}Ga_{0.50}As$ quantum wells. Cases are shown for which valence-subband configurations are heavy-hole up by ~ 2 meV, merged, and light-hole up by ~ 2 meV. Conventions are the same as those used in Fig. 4. Note that thin barriers favor a light-hole-up valence-subband configuration in these structures, contrary to the SLS's of Fig. 8 in which strain sharing between wells and barriers resulted in the opposite trend.

tial changes in the optical matrix elements at finite $\mathbf{k}_{\|}$ which result from only a 4-meV net shift in the relative positions of the uppermost light- and heavy-hole subbands. Note also that increasing the barrier width pushes the heavy-hole band above the light-hole band in these types of structures, contrary to the SLS's of Fig. 8 in which sharing of strain between the layers yielded the opposite trend. It should be noted that the total superlattice thickness must be kept below some critical value in structures of this type if dislocations are to be avoided, since the superlattice as a whole is not lattice matched to the substrate. This superlattice critical thickness can be relatively large, however, for cases such as the one examined here in which the overall mismatch is small.

IV. SUMMARY AND CONCLUSIONS

In this paper, we have described a systematic theoretical study of the effects of tensile strain on the band structures and optical matrix elements of semiconductor quantum wells (QW's) and strained-layer superlattices (SLS's). We first described finite-element and superlattice $\mathbf{K}\cdot\mathbf{p}$ models which we used in our work to study strained single quantum wells and strained superlattices, respectively, and compared results from these two models for thick barrier superlattices in which the quantum wells are decoupled. Band structures obtained from the two models were shown to be in generally excellent quantitative agreement near the zone center and strong qualitative agreement at larger wave vectors, despite formal differences in the two models and selection of test cases in which interband interactions should be particularly strong.

We then applied the finite-element model to isolated strained quantum wells, beginning with calculations of the well-width dependence of electron–light-hole (e-lh) and electron–heavy-hole (e-hh) optical transition energies in $GaAs_{1-x}P_x/Al_{0.35}Ga_{0.65}As$ and $In_xGa_{1-x}As/InP$ structures of various alloy compositions. Results of these studies showed that the heavy-hole-up valence-subband configuration characteristic of lattice-matched and compressively strained quantum wells is available in tensile-strained wells only below some composition dependent well thickness, and that this characteristic thickness decreases rapidly with increasing tensile strain. Energy bands and wave-vector-dependent optical matrix elements were then studied for both systems in regimes where variation of quantum-well widths or compositions induce merging and reversal of the uppermost light- and heavy-hole bands. Our results show significant changes in band structures and matrix elements with tuning of the subband configuration through the merger point, including reversal of the signs of effective masses for both types of holes and drastic changes in optical matrix elements at small finite values of in-plane wave vector. Similar results were obtained whether bands were tuned through the merger point by variation of quantum-well width or alloy composition for both $GaAs_{1-x}P_x/Al_{0.35}Ga_{0.65}As$ and $In_xGa_{1-x}As/InP$ structures. One particularly notable result is that the TM optical matrix elements become strongly enhanced for electron–light-hole transitions and strongly suppressed for electron–heavy-hole transitions over a wide range of wave vectors in tensile-strained quantum wells with light-hole-up valence-band configurations. This is interesting in light of recent data showing strong TM polarization of lasers utilizing quantum wells with such band configurations, which presumably operate primarily on electron–light-hole transitions.

Finally, we applied the superlattice $\mathbf{K}\cdot\mathbf{p}$ model to structures in the same material systems in which merging and reversal of the bands is induced by variation of barrier width alone. Free-standing $GaAs_{1-x}P_x/Al_yGa_{1-y}As$ superlattices with strain shared between the well and barrier layers were first studied. Our results indicate that increasing barrier widths results in tuning of the subband configuration from heavy-hole-up to light-hole-up band configurations in these structures. We then studied $In_xGa_{1-x}As/InP$ structures strained to lattice matched to InP substrates, in which all strain is confined to the $In_xGa_{1-x}As$ quantum wells. Tuning the subband configuration from heavy-hole up to light-hole up requires a *decrease* in the barrier width in this case, contrary to the free-standing $GaAs_{1-x}P_x/Al_yGa_{1-y}As$ in which strain sharing resulted in the opposite trend. Valence-band crossing is shown to be achievable solely through barrier-width variations in both types of structures, and subband reversal was predicted to result in large changes in band structures and matrix elements as was found to be the case for single wells.

ACKNOWLEDGMENTS

The authors thank the National Science Foundation for their support of this work through Grants Nos. ECS-8910415 and ECS-8911995. We also thank Dr. D. Sorensen of Rice University for providing us with the eigensolver package.

APPENDIX A

The unitary transformation used in Sec. II B to transform the 6×6 valence-band Hamiltonian matrix to a block diagonal form is

$$\mathbf{U}=\begin{bmatrix} \frac{e^{-i\phi}}{\sqrt{2}} & 0 & 0 & 0 & 0 & -\frac{e^{+i\phi}}{\sqrt{2}} \\ 0 & \frac{e^{-i\eta}}{\sqrt{2}} & 0 & 0 & -\frac{e^{i\eta}}{\sqrt{2}} & 0 \\ 0 & 0 & \frac{e^{-i\beta}}{\sqrt{2}} & -\frac{e^{i\beta}}{\sqrt{2}} & 0 & 0 \\ 0 & 0 & \frac{e^{-i\beta}}{\sqrt{2}} & \frac{e^{i\beta}}{\sqrt{2}} & 0 & 0 \\ 0 & \frac{e^{-i\eta}}{\sqrt{2}} & 0 & 0 & \frac{e^{i\eta}}{\sqrt{2}} & 0 \\ \frac{e^{-i\phi}}{\sqrt{2}} & 0 & 0 & 0 & 0 & \frac{e^{i\phi}}{\sqrt{2}} \end{bmatrix}.$$

Here

$$\beta=\eta=\frac{\theta_c-\theta_b}{2}+\frac{\pi}{4}\ ,\quad \phi=\frac{\theta_b+\theta_c}{2}-\frac{\pi}{4}\ ,$$

where θ_b and θ_c are related to the parameters b and c (Eqs. 13 and 14) as $b=|b|e^{i\theta_b}$ and $c=|c|e^{i\theta_c}$ and to one another as $\theta_c=2\theta_b$. The transformed valence Bloch states are

$$|1\rangle=\frac{e^{i\phi}}{\sqrt{2}}|\tfrac{3}{2},\tfrac{3}{2}\rangle-\frac{e^{i\phi}}{\sqrt{2}}|\tfrac{3}{2},-\tfrac{3}{2}\rangle\ ,$$

$$|2\rangle=\frac{e^{-i\eta}}{\sqrt{2}}|\tfrac{3}{2},\tfrac{1}{2}\rangle-\frac{e^{i\eta}}{\sqrt{2}}|\tfrac{3}{2},-\tfrac{1}{2}\rangle\ ,$$

$$|3\rangle=\frac{e^{i\beta}}{\sqrt{2}}|\tfrac{1}{2},\tfrac{1}{2}\rangle-\frac{e^{i\beta}}{\sqrt{2}}|\tfrac{1}{2},-\tfrac{1}{2}\rangle\ ,$$

$$|4\rangle=\frac{e^{-i\phi}}{\sqrt{2}}|\tfrac{3}{2},\tfrac{3}{2}\rangle+\frac{e^{i\phi}}{\sqrt{2}}|\tfrac{3}{2},-\tfrac{3}{2}\rangle\ ,$$

$$|5\rangle=\frac{e^{-i\eta}}{\sqrt{2}}|\tfrac{3}{2},\tfrac{1}{2}\rangle+\frac{e^{i\eta}}{\sqrt{2}}|\tfrac{3}{2},-\tfrac{1}{2}\rangle\ ,$$

$$|6\rangle=\frac{e^{-i\beta}}{\sqrt{2}}|\tfrac{1}{2},\tfrac{1}{2}\rangle+\frac{e^{i\beta}}{\sqrt{2}}|\tfrac{1}{2},\tfrac{1}{2}\rangle\ .$$

APPENDIX B

Strain-dependent envelope functions at $\mathbf{K}=\mathbf{0}$ for the superlattice subband states are obtained in closed form using the superlattice $\mathbf{K}\cdot\mathbf{p}$ formalism described in Sec. II C. These functions are tabulated in this Appendix.

For a SLS with quantum-well and barrier-layer thicknesses L_A and L_B, respectively, the functions (even and odd) used to construct the superlattice $\mathbf{K}=\mathbf{0}$ states are as follows:

	$-L_A/2\le z\le L_A/2$	$L_A/2\le z\le L_A/2+L_B$
$M_J=+\frac{1}{2}$ Even	$F_{v,\|1,0\rangle}=N\cos K_A Z$	$N\dfrac{\cos k_A L_A/2}{\cos k_B L_B/2}\cos k_B(z-d/2)$
	$F_{v,\|5,0\rangle}=N\gamma_A C_{5A}\sin k_A Z$	$-N\gamma_A\dfrac{\sin k_A L_A/2}{\sin k_B L_B/2}C_{5B}\sin k_B(z-d/2)$
	$F_{v,\|7,0\rangle}=N\gamma_A C_{7A}\sin k_A z$	$-N\gamma_A\dfrac{\sin k_A L_A/2}{\sin k_B L_B/2}C_{7B}\sin k_B(z-d/2)$
$M_J=+\frac{3}{2}$ Even	$F_{v,\|3,0\rangle}=N\sin k_A Z$	$-N\gamma_A\dfrac{\sin k_A L_A/2}{\sin k_B L_B/2}C_{7B}\sin k_B(z-d/2)$
$M_J=+\frac{1}{2}$ Odd	$F_{v,\|1,0\rangle}=\dfrac{N}{\gamma_A}\sin k_A Z$	$\dfrac{-N}{\gamma_A}\dfrac{\sin k_A L_A/2}{\sin k_B L_B/2}\sin k_B(z-d/2)$
	$F_{v,\|5,0\rangle}=NC_{5A}\cos k_A Z$	$N\dfrac{\cos k_A L_A/2}{\cos k_B L_B/2}C_{5B}\cos k_B(z-d/2)$
	$F_{v,\|7,0\rangle}=NC_{7A}\cos k_A Z$	$N\dfrac{\cos k_A L_A/2}{\cos k_B L_B/2}C_{7B}\cos k_B(z-d/2)$
$M_J=+\frac{3}{2}$ Odd	$F_{v,\|3,0\rangle}=N\cos k_A Z$	$N\dfrac{\cos k_A L_A/2}{\cos k_B L_B/2}\cos k_B(z-d/2)$

where $\gamma_A=[\sqrt{3}E_L(k=0)m_0/P\hbar k_A]$, m_0 is the free electron mass, d is the superlattice period ($d=L_A+L_B$), N is the appropriate normalization constant, and k_A and k_B are the bulk (z-d directed) wave vectors in the A and B layers, respectively.

The constants C_{5B} and C_{7B} are

$$C_{5B}=\frac{\sqrt{2}\left[E_L(K=0)+E_g+Aa_c\varepsilon-Aa_v\varepsilon-\dfrac{\left[\dfrac{\sqrt{2}Bb_v\varepsilon}{3}+\dfrac{\varepsilon\Delta}{9\sqrt{2}}\right]^2}{\Delta+Bb_v\varepsilon/3}\right]-V_S(z)}{3E_L(K=0)+3E_g+2\Delta+3Aa_c\varepsilon-3Aa_v\varepsilon+\dfrac{Bb_v\varepsilon}{3}-\dfrac{\left[\dfrac{\sqrt{2}Bb_v\varepsilon}{3}+\dfrac{\varepsilon\Delta}{9\sqrt{2}}\right]^2}{\Delta+\dfrac{Bb_v\varepsilon}{3}}-2V_S(z)}\ ,$$

$$C_{7B}=\frac{\sqrt{2}\left[E_L(k=0)+E_g+Aa_c\varepsilon-Aa_v\varepsilon+\frac{Bb_v\varepsilon}{3}+\frac{2\left[\sqrt{2}\frac{Bb_v\varepsilon}{3}+\frac{\varepsilon\Delta}{9\sqrt{2}}\right]}{\Delta+Bb_v\varepsilon/3}\right]-V_1(z)}{3E_L(K=0)+3E_g+2\Delta+3Aa_c\varepsilon-3Aa_v\varepsilon+\frac{Bb_v\varepsilon}{3}-\frac{\left[\frac{\sqrt{2}Bb_v\varepsilon}{3}+\frac{\varepsilon\Delta}{9\sqrt{2}}\right]^2}{\Delta+Bb_v\varepsilon/3}-2V_S(z)-V_1(z)},$$

where $V_S(z)$ and $V_1(z)$ are step functions which vanish in the A layers and are equal to the band offsets for split-off and light-hole bands, respectively, in the B layers, and E_g is the bandgap of the A material. Finally, it follows that

$$C_{5A}=C_{5B}\Big|_{V_S,V_1=0},\quad C_{7A}=C_{7B}\Big|_{V_S,V_1=0}.$$

APPENDIX C

Material parameters used in the calculations of this work are

	$GaAs_{1-x}P_x$	$Al_yGa_{1-y}As$	$In_xGa_{1-x}As$	InP	Units
E_g	$1.514+1.17x+0.19x^2$ (77 K)	$1.5076+1.247y$ (77 K)	$0.324+0.7(1-x)+0.4(1-x)^2$ (300 K)	1.344 (300 K)	eV
m_e	$0.17-0.103(1-x)$	$0.15y+0.067(1-y)$	$0.0219x+0.067(1-x)$	0.079	m_0
$m_{hh\langle 100\rangle}$	$0.79-0.45(1-x)$	$0.4785y+0.4082(1-y)$	$0.2631x+0.408\,16(1-x)$	0.520 83	m_0
$m_{hh\langle 111\rangle}$	$0.67x+0.813(1-x)$	$0.87y+0.813(1-y)$	$0.4545x+0.813(1-x)$	0.6329	m_0
m_{lh}	$0.14-0.048(1-x)$	$0.2079y+0.087\,34(1-y)$	$0.027x+0.0873(1-x)$	0.122 54	m_0
a	$5.4505x+5.653\,25(1-x)$	$5.66y+5.653\,25(1-y)$	$6.0583x+5.653\,25(1-x)$	5.8679	Å
Δ	$0.08x+0.34(1-x)$	$0.28y+0.34(1-y)$	$0.38x+0.34(1-x)$	0.11	eV
C_{11}	$1.414x+1.19(1-x)$	$1.25y+1.19(1-y)$	$0.83x+1.22(1-x)$	1.02	$\times 10^{10}\ \frac{dyn}{cm^2}$
C_{12}	$0.6398x+0.538(1-x)$	$0.53y+0.538(1-y)$	$0.45x+0.57(1-x)$	0.58	$\times 10^{10}\ \frac{dyn}{cm^2}$

Luttinger parameters are related to the effective masses as

$$\gamma_1=\frac{1}{2}\left[\frac{1}{m_{lh}}+\frac{1}{m_{hh\langle 100\rangle}}\right],\quad \gamma_2=\frac{1}{4}\left[\frac{1}{m_{lh}}-\frac{1}{m_{hh\langle 100\rangle}}\right],\quad \gamma_3=\frac{1}{2}\left[\gamma_1-\frac{1}{m_{hh\langle 111\rangle}}\right].$$

[1]D. C. Bertolet, J.-K. Hsu, and K. M. Lau, Appl. Phys. Lett. **53**, 2501 (1988).

[2]See, for example, L. F. Tiemeijer, P. J. A. Thijs, P. J. de Waard, J. J. Binsma, and T. v. Dongen, Appl. Phys. Lett. **58**, 2738 (1991); C. E. Zah, R. Bhat, B. Pathak, C. Caneau, F. J. Favire, N. C. Andreadakis, D. M. Hwang, M. A. Koza, C. Y. Chen, and T. P. Lee, Electron. Lett. **27**, 1414 (1991).

[3]K. Magari, M. Okamoto, H. Yasaka, K. Sato, Y. Noguchi, and O. Mikami, IEEE Photon Technol. Lett. **2**, 556 (1990); M. Joma, H. Horikawa, C. Q. Xu, K. Yamada, Y. Katoh, and T. Kamijoh, Appl. Phys. Lett. **62**, 121 (1993).

[4]Y. Chen, J. E. Zucker, N. J. Sauer, and T. Y. Chang, IEEE Photon Technol. Lett. **4**, 1120 (1992).

[5]B. N. Gomatam and N. G. Anderson, IEEE J. Quantum Electron. **QE-28**, 1496 (1992); B. N. Gomatam, N. G. Anderson, F. Agahi, C. F. Musante, and Kei May Lau, Appl. Phys. Lett. **63**, 3616 (1993).

[6]M. Altarelli, in *Interfaces, Quantum Wells, and Superlattices,* edited by C. R. Leavens and Roger Taylor (Plenum, New York, 1987), pp. 43–66.

[7]J. M. Luttinger and W. Kohn, Phys. Rev. **97**, 869 (1955).

[8]J. M. Luttinger, Phys. Rev. **102**, 1030 (1956).

[9]G. E. Pikus and Cr.L. Bir, Fiz. Tverd. Tela (Leningrad) **1**, 154 (1959) [Sov. Phys. Solid State **1**, 136 (1959)]; **1**, 1642 (1959) [**1**, 1502 (1960)].

[10]N. G. Anderson and S. D. Jones, J. Appl. Phys. **70**, 4342 (1991).

[11]See, for example, M. Altarelli, in *Heterojunctions and Semiconductor Superlattices,* edited by G. Allan, G. Bastard, N. Boccara, M. Lannoo, and M. Voos (Springer-Verlag, Berlin, 1986), p. 15

[12]K. Nakamura, A. Shinizu, M. Koshiba, and K. Hayata, IEEE J. Quantum Electron. **25**, 889 (1989).

[13]D. C. Sorensen, SIAM J. Matr. Anal. Apps. **13**, 357 (1992).

[14]N. F. Johnson, H. Ehrenreich, P. M. Hui, and P. M. Young, Phys. Rev. B **41**, 3655 (1990).
[15]P. M. Young, Ph.D. thesis, Harvard University, 1992.
[16]M. Wagner, *Unitary Transformations in Solid State Physics* (North-Holland, New York, 1986), p. 88.
[17]*Semiconductors and Semimetals,* Vol. 32, edited by T. P. Pearsall (Academic, New York, 1990), p. 68.
[18]Experimental evidence of this mass reversal has recently been reported in L. Vina, L. Munoz, N. Mestres, E. S. Koteles, A. Ghiti, E. P. O'Reilly, D. C. Bertolet, and K. M. Lau, Phys. Rev. B **47**, 13 926 (1993).
[19]See, for example, Atul Mathur, Julian S. Osinski, Piotr Grodzinski, and P. Daniel Dapkus, IEEE Photon. Technol. Lett. **5**, 753 (1993).